Geophysical Research Letters

RESEARCH LETTER
10.1029/2019GL084926

Key Points:
- The 20 May 2016 M_w 6.0 Petermann Ranges earthquake, Australia resulted from reverse faulting
- Iterative Closest Point (ICP) comparison of preearthquake and postearthquake DEMs derived from optical satellite imagery
- A 21-km-long rupture with maximum vertical deformation of 0.7 m and broad 0.5- to 1-km-wide deformation zone

Supporting Information:
- Supporting Information S1
- Data Set S1

Correspondence to:
R. D. Gold,
rgold@usgs.gov

Citation:
Gold, R. D., Clark, D., Barnhart, W. D., King, T., Quigley, M., & Briggs, R. W. (2019). Surface rupture and distributed deformation revealed by optical satellite imagery: The intraplate 2016 M_w 6.0 Petermann Ranges earthquake, Australia. *Geophysical Research Letters*, *46*. https://doi.org/10.1029/2019GL084926

Received 12 AUG 2019
Accepted 22 AUG 2019
Accepted article online 29 AUG 2019

Surface Rupture and Distributed Deformation Revealed by Optical Satellite Imagery: The Intraplate 2016 M_w 6.0 Petermann Ranges Earthquake, Australia

Ryan D. Gold[1], Dan Clark[2], William D. Barnhart[3], Tamarah King[4], Mark Quigley[4], and Richard W. Briggs[1]

[1]U.S. Geological Survey, Golden, CO, USA, [2]Geoscience Australia, Symonston, ACT, Australia, [3]Department of Earth and Environmental Sciences, University of Iowa, Iowa City, IA, USA, [4]School of Earth Sciences, University of Melbourne, Melbourne, Victoria, Australia

Abstract High-resolution optical satellite imagery is used to quantify vertical surface deformation associated with the intraplate 20 May 2016 M_w 6.0 Petermann Ranges earthquake, Northern Territory, Australia. The 21 ± 1-km-long NW trending rupture resulted from reverse motion on a northeast dipping fault. Vertical surface offsets of up to 0.7 ± 0.1m distributed across a 0.5-to-1-km-wide deformation zone are measured using the Iterative Closest Point algorithm to compare preearthquake and postearthquake digital elevation models derived from WorldView imagery. The results are validated by comparison with field-based observations and interferometric synthetic aperture radar. The pattern of surface uplift is consistent with distributed shear above the propagating tip of a reverse fault, leading to both an emergent fault and folding proximal to the rupture. This study demonstrates the potential for quantifying modest (<1 m) vertical deformation on a reverse fault using optical satellite imagery.

1. Introduction

Reverse faulting earthquakes in continental crust can create complex surface rupture patterns, including large step overs and combinations of discrete and distributed deformation (e.g., 1978 Tabas-e-Golshan, Iran, Berberian, 1979; 2001 Bhuj, India, Bodin & Horton, 2004; 1994 Northridge, United States, Hudnut et al., 1996; 1980 El Asnam, Algeria, Philip & Meghraoui, 1983; 2008 Wenchuan, China, Xu et al., 2009). Reverse faults pose a significant seismic hazard to several large population centers on Earth and are often difficult to identify at the surface (e.g., Tehran, Taipei, Kathmandu, Kabul, and Los Angeles; Bilham, 2009; Dolan et al., 2003). To better constrain empirical relationships between surface rupture, displacement, and earthquake magnitude (Wells & Coppersmith, 1994) and forecasts of earthquake-induced surface deformation fields relevant to engineering design and land use planning (Moss & Ross, 2011a), improved knowledge of the surface deformation induced by reverse faulting earthquakes is required. This can be achieved by high-resolution documentation of ground-rupturing earthquakes.

The slowly eroding, low-relief, sparsely vegetated and sparsely populated landscapes of Australia present a rare opportunity to investigate both reverse fault ground surface ruptures and subtle distributed deformation features, which is more challenging in many other settings (Quigley et al., 2010). Field-based approaches (e.g., field mapping and surveying) have been used to document surface ruptures from recent Australian earthquakes (e.g., Bowman & Barlow, 1991; Clark et al., 2013; Crone et al., 1992; Machette et al., 1993). However, ruptures in remote regions are logistically challenging to map, and broad deformation is difficult to capture in the absence of man-made linear features. Remote sensing techniques provide powerful tools to augment traditional field-based mapping, but they also have limitations. For example, interferometric synthetic aperture radar (InSAR) captures a single displacement vector in the radar line of sight (LOS; primarily vertical; Massonnet et al., 1993; Simons et al., 2002) but commonly decorrelates in regions close to earthquake surface ruptures where displacement gradients exceed the Nyquist sampling rate or cause pixels to no longer overlap (e.g., Hamling et al., 2017; Metzger et al., 2017). Additionally, image cross-correlation approaches (i.e., pixel tracking) quantify horizontal components of displacement via comparison of preeathquake and postearthquake images (e.g., Barnhart et al., 2015; Hollingsworth et al., 2017; Klinger et al., 2006, 2018; Leprince et al., 2007; Milliner et al., 2015), but traditional approaches do not resolve the vertical component of surface deformation and have uncertainties of 1–2 orders of magnitude greater than InSAR.

A number of recent studies quantify vertical surface deformation associated with ground-rupturing earthquakes based on combinations of lidar, aerial photographs, satellite imagery, and InSAR data (Avouac & Leprince, 2015; Barnhart et al., 2019; Kuo et al., 2018; Nissen et al., 2014; Oskin et al., 2012; Scott et al., 2019; Zhou et al., 2018). This study contributes to this emerging field using high-resolution optical satellite imagery to measure vertical coseismic surface displacements produced by the 20 May 2016 M_w 6.0 Petermann Ranges earthquake, Northern Territory, Australia. We compare preearthquake and postearthquake digital elevation models (DEMs) derived from high-resolution optical satellite imagery to quantify vertical surface deformation associated with a surface rupturing earthquake. This analysis reveals a broad zone of hanging-wall deformation, which we interpret to have resulted from slip dissipation away from the primary rupture plane as the rupture approached the surface, leading to a combination of both an emergent fault and broadly distributed deformation local to the rupture.

2. Geologic Background

The 20 May 2016 M_w 6.0 Petermann Ranges earthquake occurred in remote central Australia (King et al., 2018; Polcari et al., 2018; Wang et al., 2019). The epicenter was located ~120 km west-southwest of Yulara (Uluru) in the sparsely populated southwest corner of the Northern Territory, Australia (Figure 1). InSAR modeling suggests that the source fault dips 22–39° to the northeast and that the earthquake produced largely reverse motion with a minor left-lateral component of slip (Polcari et al., 2018; Wang et al., 2019). Maximum slip derived from InSAR modeling was ~1 m and occurred at shallow depths, <3–4 km (Polcari et al., 2018; Wang et al. 2019). Polcari et al. (2018) conclude that the causative fault is a back thrust that soles into the NW-striking, SW dipping Woodroffe thrust fault, a structure associated with the late Proterozoic to Cambrian Petermann orogeny (Camacho et al., 1995; Edgoose et al., 2004).

The interior of Australia is considered tectonically quiescent given its distance from plate boundaries and lack of geodetically resolvable internal strain (Tregoning, 2003). Despite its intraplate setting, Australia has experienced a number of notable historical earthquakes, which are thought to result from far-field plate boundary forces that have exploited preexisting structures in the continental crust of Australia (Clark et al., 2012). The most significant of these surface rupturing historical earthquakes include the 1968 M_s 6.8 Meckering earthquake (Gordon & Lewis, 1968), the 1986 M_s 5.8 Marryat Creek earthquake (Bowman & Barlow, 1991; Crone et al., 1997; Machette et al., 1993), and the 1988 Tennant Creek earthquake sequence, which included a M_w 6.6 earthquake (Bowman, 1992; Crone et al., 1992, 1997).

3. Methods

3.1. Surface-Rupture Mapping

We used two postearthquake WorldView-3 (©2019, DigitalGlobe), orthorectified ~0.3-m resolution images to remotely map the primary ground surface rupture and subsidiary fault traces and lineaments at a scale of 1:5,000 (Table S1). The fault rupture could not be recognized in the optical imagery in areas covered by dunes (Figure S1), and where scarps were <10- to 15-cm high or not oriented such that they cast a sharp shadow. The remotely mapped surface rupture traces are included as a KML file in the supporting information.

3.2. WorldView-Derived Digital Elevation Models

We generated DEMs using preevent and postevent in-track stereo 0.5-m resolution panchromatic WorldView-1 and WorldView-2 images (©2019, DigitalGlobe) using the Surface Extraction from TIN-based Searchspace Minimization software (Noh & Howat, 2015) running on the University of Iowa Argon supercomputer (Table S1, DEMs available at https://doi.org/10.5066/P9353101). The postevent DEMs exhibit along-track striping artefacts common to the WorldView 2 sensor. While destriping tools, for example, within National Aeronautics and Space Administration's Ames Stereo Pipeline (Shean et al., 2016), are commonly applied to resolve this issue, a destriping correction has not been developed for this latitude. We used the Iterative Closest Point (ICP) algorithm to find the coseismic vertical displacement field from our preevent and postevent DEMs (Figure 1; e.g., Barnhart et al., 2019; Besl & McKay, 1992; Nissen et al., 2012). ICP yields horizontal and displacement fields, and rotations by matching three-dimensional features (topography) between DEMs. Details on the DEM-generation methods and ICP calculations are described in the supporting information (Text S1).

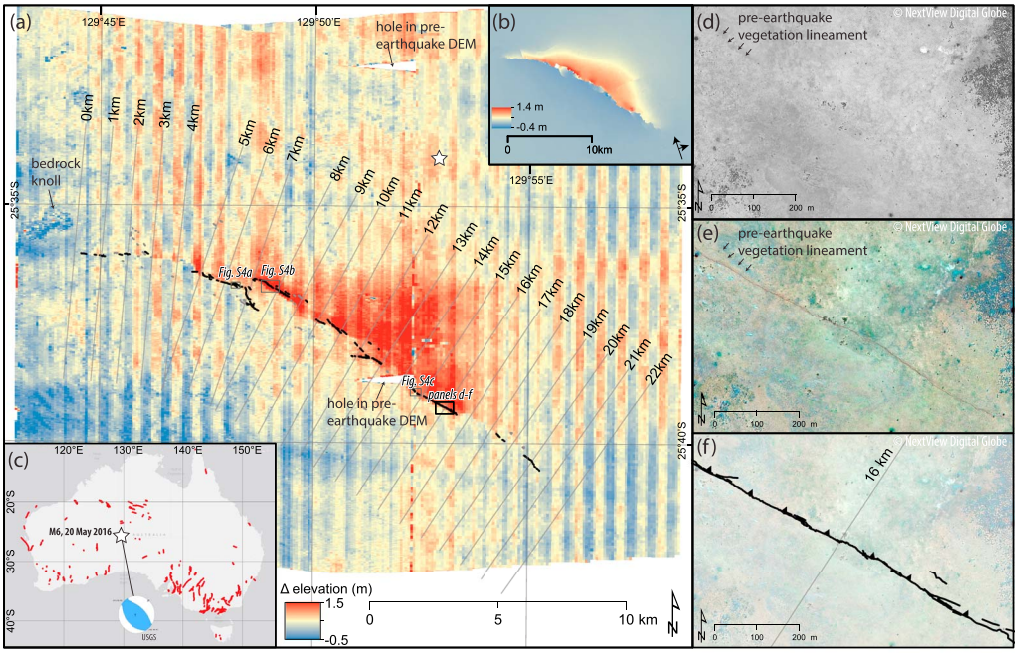

Figure 1. (a) Coseismic vertical displacement field measured from the Iterative Closest Point algorithm comparison of digital elevation models derived from pre-earthquake and postearthquake WorldView imagery overlain with mapped fault traces (black lines) and lineaments (gray lines). Vertical striping from known problem with WorldView-2 sensor that cannot be easily corrected at this latitude. The color scale is saturated at +1.5/−0.5 m. (b) Line-of-sight interferogram derived from ALOS-2 interferometric synthetic aperture radar (15 December 2015 to 14 June 2016, ascending orbit), with range and azimuth direction illustrated. (c) Location map showing epicenter (star) and focal mechanism of 20 May 2016 M_w 6.0 Petermann Ranges earthquake and mapped faults that are younger than 5–10 Ma (www.ga.gov.au/applications/neotectonic-features-database, last accessed 6 April 2018). (d) Preearthquake, (e) postearthquake, and (f) interpreted WorldView-3 image (©2019, DigitalGlobe) showing location of surface rupture at kilometer 16. A preearthquake vegetation lineament that is near the rupture trace is mapped and is unrelated to faulting. Additional preearthquake and postearthquake optical images are presented in the electronic supplement to this article (Figure S4).

To quantify vertical surface displacement along the length of the rupture, we extracted 10-km-long swath profiles from the residual DEM, spaced 1 km apart along and orthogonal to the rupture trace. The swath profiles sample and average the topography ±500 m from the profile line to resolve signal in the noisy residual DEM (Figures 2 and S3). Vertical separation measurements are calculated from the minimum/maximum values from each side of the fault and broader zone of distributed folding (typically ±500 m from primary rupture). We employed a range of linear regressions fit to the residual DEM to estimate the uncertainty for each vertical separation measurement, typically 0.2–0.3 m (>20–30% of total measurement).

3.3. Field Measurements

A team of Australia-based researchers deployed to the field within a month following the earthquake (King et al., 2018). They documented the surface rupture and measured vertical separation across the fault. The field survey provided an independent check of the remote rupture fault-trace mapping based on WorldView-3 imagery, described above. Qualitatively, there is excellent agreement between fault traces identified in the field and remotely.

The field-based vertical separation measurements included 19 fault-perpendicular profiles 30-to-500-m long across the fault scarp and 85 measurements from the base and top of the fault scarp (Table S4). For the fault-perpendicular profiles, the preexisting ground surface was projected into the fault zone to determine vertical separation, whereas the base/top of fault scarp measurements were simply differenced to estimate vertical separation. All measurements were made with a real-time kinematic GPS and are associated with horizontal and vertical uncertainties of <2 cm. The western 5 km of the rupture was not characterized because the surface expression of this section was predominantly a series of distributed cracks overlying a broad belt of shear that could not be defined. Difficulties were encountered in measuring vertical displacement across the scarp

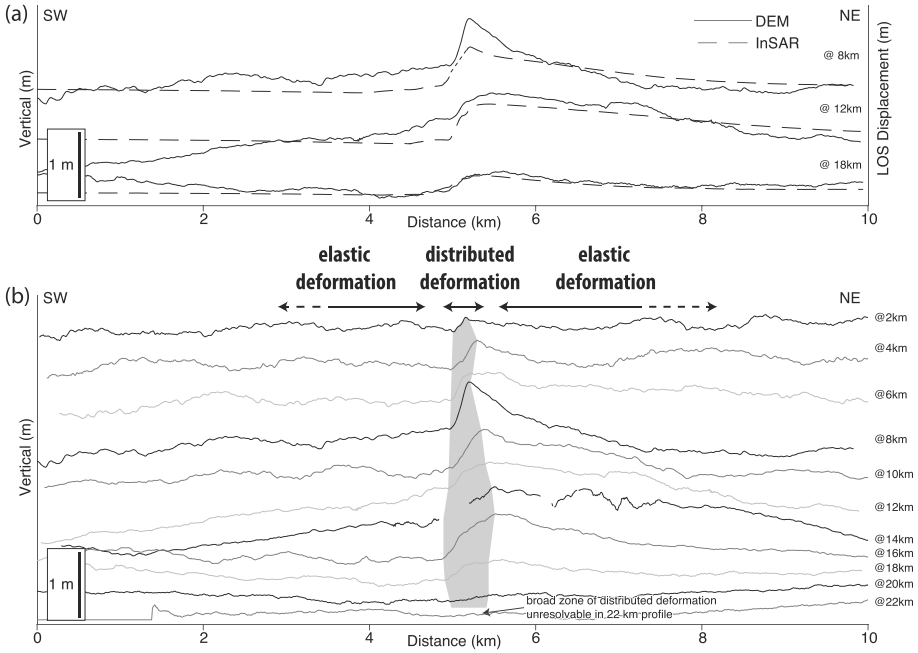

Figure 2. Profiles of surface deformation, orthogonal to rupture trace (profile locations on Figure 1). Profiles vertically and horizontally offset arbitrarily to facilitate comparison. (a) Comparison of differenced digital elevation model (DEM) using Iterative Closest Point algorithm and line-of-sight displacement from ALOS-2 interferometric synthetic aperture radar (InSAR) at kilometers 8, 12, and 18. A direct comparison of the DEM and InSAR measurements is not possible because the InSAR measurements are LOS. (b) Average of 1-km-wide swath profiles extracted from the residual of the differenced preearthquake and postearthquake DEMs, orthogonal to the rupture trace. Gray polygon delineates broad 0.5-to-1-km-wide zone of broadly distributed deformation local to the rupture, which we speculate resulted from slip dissipation as the rupture approached the surface. A compilation of all profiles derived from the InSAR (Figure S2) and the residual DEMs (Figure S3) are provided in the supporting information.

where the rupture crossed sand dunes. This caused incomplete coverage of measurements as compared to the differenced DEM and InSAR results. Irrespective, where available, we use the vertical separation documented from the field measurements to validate the results from the ICP comparison of the DEMs.

3.4. InSAR

We generated a coseismic interferogram from the JAXA ALOS-2 PALSAR L-band instrument (15 December 2015 to 14 June 2016, ascending orbit). This analysis largely reproduces previously published results (Polcari et al., 2018; Wang et al., 2019). Details on data processing are provided in the electronic supplement. The results presented here are LOS displacements that include both vertical and horizontal components of displacements (Figure 1b); accordingly, we only use these results for qualitative comparison to the differenced DEMs.

4. Results

4.1. Surface Rupture

Mapping of the primary surface rupture using WorldView-3 imagery reveals a 21 ± 1-km-long, NW-trending, arcuate, southwest facing fault trace. The trace broadly comprises three sections (Figure 1). The eastern section of the surface rupture (kilometer 17 to 22) is linear and mostly single-stranded with southwest-facing scarps. It is discontinuous in places where it passes through <8-m amplitude sand dunes (Figure S1). The ICP analysis and InSAR results, described below, demonstrate that the rupture continues through these locations; however, it is not visible as a discrete rupture due to dispersion of deformation within the noncohesive sand. The central portion of the rupture (kilometer 7.5 to 17) comprises several strands as the rupture curves to a more E-W orientation to the west. The central section of the rupture overlaps by approximately 1 km between 7 and 8 km with the western section (kilometers 0 to 7.5), which is distributed, multistranded, and discontinuous.

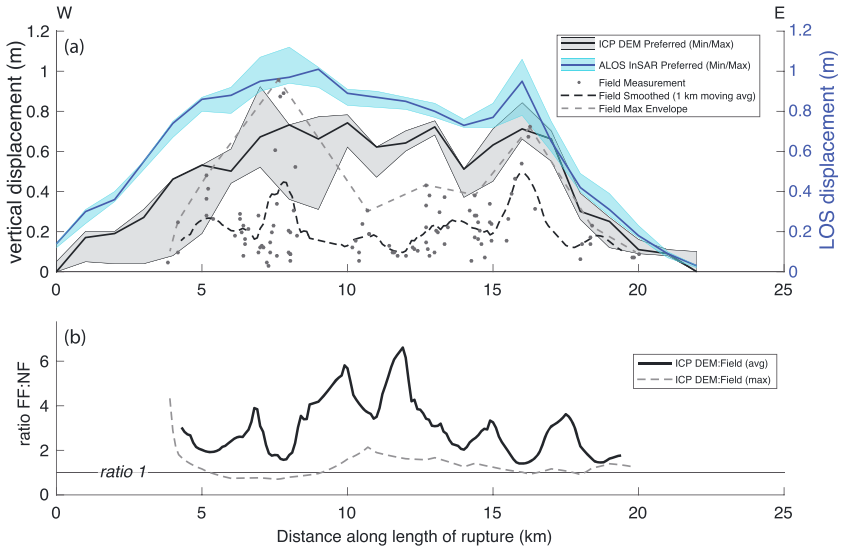

Figure 3. (a) Vertical displacement curves and error envelopes from Iterative Closest Point (ICP) comparison of preearthquake and postearthquake digital elevation models (DEMs), line-of-sight (LOS) displacement from interferometric synthetic aperture radar (InSAR), and field measurements. In general, the differenced DEM and LOS displacements measured from InSAR are larger than the field measurements. However, a maximum envelope fit to the field measurements (dashed gray line) yields reasonable agreement. (b) Ratio of field measurements to the differenced DEM measurements, including the 1-km moving average and the maximum envelope.

Analysis of the preearthquake imagery and DEM does not reveal a preexisting scarp (Figures 1d and S4), consistent with reconnaissance excavations across the fault trace (D. Clark, written communication, 2018). This observation suggests that the Petermann earthquake rupture occurred on a fault that has not generated ground surface rupture with sufficient frequency and finite displacement to outpace bedrock erosion rates.

4.2. Differenced DEM Surface Deformation

The ICP comparison reveals minor footwall deformation (downwarping) and more significant deformation (upwarping) in the hanging wall, which extends >4 km from the rupture trace (Figure 1). There are several anomalies in the residual DEM, for example triangular artefacts that resulted when creating a DEM from the WorldView imagery and vertical stripes, described above.

Analysis of the swath profiles reveals a 0.5-to-1-km-wide zone of distributed faulting and folding resulting from broader shear centered on the primary surface rupture trace (Figure 2). In the footwall, downward warping can be observed up to 3 km from the rupture. In the hanging wall, upward warping is observed >4 km from the rupture trace. Analysis of the along-strike vertical surface separation (Figure 3) reveals a generally smoothly varying, half-elliptical form (Pollard & Segall, 1987). A maximum preferred displacement of 0.7 ± 0.1 m extends from 8-to-16 km along the length of the rupture. Displacement peaks are observed at kilometers 8, 12-to-13, and 16. Average vertical displacement over the length of the rupture is 0.4 ± 0.3 m.

4.3. InSAR Results

The LOS displacements measured from the InSAR (Figure 1b) show a far-field deformation pattern associated with shallow faulting extending for ~20 km and closely corresponds with our surface rupture mapping. The InSAR data show minor LOS increases in the footwall, which we interpret as downwarping of the footwall near the rupture, and more significant hanging wall deformation extending for up to 10 km for the rupture trace (evidenced as LOS decrease or motion towards the satellite; Figures 1b and 2a and S2). The profiles also reveal a zone of distributed folding centered on the rupture. Maximum vertical LOS displacement reaches ~1.0 m at kilometers 9 and 16 along the length of the rupture (Figures 3a).

4.4. Field Measurements

Vertical separations measured in the field between kilometers 5 and 20 are depicted in Figure 3a. A maximum vertical separation measurement of 0.96 m was made at kilometer 7.6. However, average vertical separations range between 0.2 and 0.3 m. We fit a 1-km smoothed moving average to the field measurements (1-to-20 measurements per kilometer), which matches the spacing of our differenced-DEM measurements. We also manually fit an envelope of maximum slip to a subset of these measurements ($n = 10$, Figure 3b), which is a typical treatment of field measurement data used to compute slip distributions (e.g., Haeussler et al., 2004). Based on comparison to the InSAR and differenced DEM measurements, discussed below, we argue the maximum envelope more accurately reflects net, far-field vertical displacement associated with the earthquake.

5. Discussion

5.1. Comparison of Differenced DEM to Field and InSAR Measurements

The ICP comparison of the DEMs, the field measurements, and InSAR yield overall similarities in the magnitude and pattern of surface deformation (Figure 3). However, the ICP analysis yields larger vertical displacement values than the field measurements. This is especially true when considering the 1-km moving average of the field measurements. However, the maximum envelope of the field measurements yields much closer agreement between the two data sets. We quantify the difference between the field measurements and the differenced DEM by calculating the along-strike ratio (Figure 3b). The average ratio of vertical displacements in the differenced DEM to the 1-km moving average of the field measurements is 3.0. By contrast, the average ratio between the differenced DEM to the maximum envelope of the field measurements is 1.3, indicating much closer agreement. The difference in measured vertical displacements may in part reflect continued postseismic displacement that is captured by the postevent DEMs that were acquired 5–6 months after the earthquake compared to field measurements made within a month of the event. However, postseismic afterslip typically composes only a small percentage of overall coseismic surface displacement (e.g., Kaneko & Fialko, 2011). In this case, Wang et al. (2019) document a maximum of 10 cm of postseismic afterslip, which is approximately 10–15% of the total.

We compare displacement values between the ICP comparison of the DEMs and the InSAR results (Figures 2a and 3). As noted previously, the InSAR results are LOS displacements, which include both horizontal and vertical displacements, so a direct comparison is not possible. However, a qualitative comparison of the form (shape) of the profiles can be employed, under the assumption that there is little along-strike variability in the kinematics of the rupture. The selected profiles shown in Figure 2a reveal DEM and InSAR displacements with similar form and magnitudes of surface displacement. Despite the swath profile averaging, the DEM results are still affected by noise. This is due in large part to the vertical striping in the WorldView-2-derived DEM. In our comparison of the along-strike displacement (Figure 3), the differenced DEM and InSAR yield similarly shaped half-elliptical displacement profiles, with minimal displacement at 0 and 22 km and a broad displacement plateau from kilometer 8 to 16. Peak displacement values at kilometer 8 and 16 and a displacement minimum at kilometer 15 are observed in both data sets.

The surface rupture documented with all methods shows vertical displacement that exceeds predictions made by typical magnitude-length scaling relationships (Wells & Coppersmith, 1994). Specifically, maximum and average displacements of 1.0 and 0.44 m, respectively, corresponds to a surface-rupture length of ~27 and 26 km based on an all-fault regression (Wells & Coppersmith, 1994).

5.2. Broad Zone of Deformation

This investigation offers insight into distributed faulting and folding associated with the rupture. Previous studies have shown that such distributed ("off-fault") deformation can account for ~15–60% of the total deformation associated with fault rupture (e.g., Gold et al., 2015; Gray et al., 2017; Milliner et al., 2015; Oskin et al., 2007; Rockwell et al., 2002; Van Dissen et al., 2013; Zinke et al., 2014), though studies have focused primarily on strike-slip faults.

The distributed pattern associated with the 2016 Petermann Ranges earthquake rupture is evident in the fault-perpendicular profiles (Figure 2), which reveal a zone of warping that extends several hundred meters from the primary fault rupture. Deformation is asymmetric, with more deformation in the hanging wall and

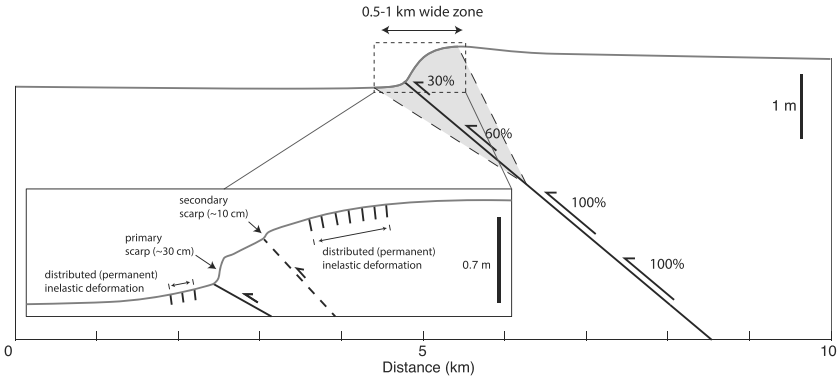

Figure 4. Schematic illustration of vertical deformation associated with shallow reverse faulting, including primary surface rupture and a zone of distributed permanent (inelastic) deformation. Decreasing slip in the shallow subsurface (gray triangular polygon), represented as a decrease in the percentage and length of slip arrow, results in a broad zone of distributed deformation. Inset figure depicts detailed view of deformation, including surface rupture on the primary fault and a secondary fault, as well as distributed deformation that results from some combination of penetrative brittle faulting, grain rotations, and other inelastic processes resulting in permanent deformation.

less in the footwall. This signal was previously recognized in the residuals from a slip model derived from InSAR (Wang et al., 2019). The ICP analysis in our investigation quantifies the near-fault signal and shows that the deformation cannot be explained solely by elastic deformation and displacement corresponding with fault scarps. We interpret the deformation profiles to record some combination of elastic and inelastic (permanent) distributed deformation (Figure 4; Kaneko & Fialko, 2011).

The broad deformation pattern is similar to observations from blind reverse fault earthquakes (Allmendinger, 1998; Champion et al., 2001; Gold et al., 2006; Streig et al., 2007). However, the 2016 Petermann Ranges earthquake produced surface rupture, indicating that the fault tip is emergent (not blind), as in a traditional trishear model. We speculate that slip dissipated as the rupture approached the surface, leading to a combination of both an emergent fault and broadly distributed deformation local to the rupture (Figure 4). Mechanical properties of the shallow crust could explain this type of slip dissipation, for example, if the rupture propagated from a mechanically weaker fault at depth to a frictionally stronger fault in the near surface. We also observe along-strike variability in the width of the deformation zone (Figure 2).

In the Petermann Ranges earthquake, bedrock is within a few meters of the ground surface (King et al., 2018), which demonstrates that distributed faulting can occur in the absence of thick alluvial cover. We recognize significant along-strike variability in the nature of the off-fault deformation signal (Figure 3b), indicating that other factors such as changes in fault strike and subsurface fault geometry may also exhibit first-order control on off-fault deformation fields.

This result is consistent with observations from paleoseismic observations made across reverse faults, where displacement at the emergent fault or shallowly buried fault tip (<100 m below surface) is often less than slip recorded by strain markers measured at length scales of tens to hundreds of meters from the emergent fault tip (Amos et al., 2011; Kelson et al., 1996; Streig et al., 2007). These relationships lead to ambiguity as to the whether the larger far-field displacements result solely from coseismic slip or from some combination of coseismic, interseismic, and/or aseismic slip. Importantly, results from our investigation capture the total coseismic deformation field from a single earthquake. While there may be a modest (<10 cm) contribution from postseismic slip (Wang et al., 2019), our results suggest that the majority of distributed vertical uplift signal observed in trenches across dip slip faults is predominantly the result of coseismic displacements.

Similarly, these results have important implications for probabilistic fault displacement hazard analysis and rotation/tilting hazard, which could influence construction setback requirements for reverse faults (Moss & Ross, 2011b). When constructing fault-perpendicular topographic profiles to measure finite vertical ground surface displacements on reverse faults in bedrock terrains, we suggest profile end points extend ≥1 km from the principal ground surface rupture trace into the hanging wall and ≥0.5 km into the footwall to capture the entire coseismic deformation signal. Increased coseismic slip and rupture complexity, and changes in

material properties of the faulted substrate, may further increase the fault-perpendicular width over which surface deformation occurs.

6. Conclusions

In this investigation, we document surface rupture and vertical deformation associated with the M_w 6.0 Petermann Ranges earthquake, Northern Territory, Australia, using remote sensing techniques. We generate preearthquake and postearthquake DEMs using in-track stereo optical satellite imagery. Comparison of the DEMs provides quantitative constraints on the vertical deformation associated with the earthquake. Comparison of these results with field-based measurements and traditional InSAR analysis demonstrates that differenced DEMs can be used to constrain vertical deformation associated with surface-rupturing earthquakes resulting in modest (<1 m) vertical motion. DEM comparisons can supplement InSAR or provide robust results for those events where InSAR data are not available. Further, the method allows for the quantification of off-fault deformation, which may not be recoverable by traditional surveying techniques, with follow-on consequences for seismic hazard studies and slip rate estimates from geologic investigations. This information has the potential to improve communal knowledge of the characteristics of earthquake-induced surface deformation and controls on how earthquake surface ruptures are expressed in the geomorphic and geologic record.

Acknowledgments
Comments provided by S. DeLong, J. Hollingsworth, K. Mueller, C. Amos, an anonymous reviewer, and Editor Jeroen Ritsema improved this study. We acknowledge the ©2019 DigitalGlobe/NextView licensing agreement, through which we accessed the preearthquake and postearthquake WorldView imagery used in this study. Data used in this investigation, specifically the digital elevation models (DEMs), are freely available at https://doi.org/10.5066/P9353101. Satellite tasking requests were processed by the National Civilian Application Center Denver/Reston and U.S. Geological Survey (USGS) Earth Resources Observation and Science (EROS) Center. ALOS-2 images were provided under JAXA award 3123: Evaluating and utilizing ALOS-2 InSAR products for international earthquake response at the USGS National Earthquake Information Center. Copernicus Sentinel data 2014–2017 retrieved from the ASF DAAC, last accessed August 2017. The USGS Earthquake Hazards Program supported this work. W. D. B. was supported by NASA ESI Award NNX16AK81G and the high-performance computational resources provided by the University of Iowa. M. Q. and T. K. thank the Australian Research Council for funding their involvement in this research under Discovery Project DP170103350. Any use of trade, product, or firm names is for descriptive purposes only and does not imply endorsement by the U.S. Government. Clark publishes with the permission of the Chief Executive Officer of Geoscience Australia.

References

Allmendinger, R. W. (1998). Inverse and forward numerical modeling of trishear fault-propagation folds. *Tectonics*, *17*(4), 640–656. https://doi.org/10.1029/98TC01907

Amos, C. B., Lapwood, J. J., Nobes, D. C., Burbank, D. W., Rieser, U., & Wade, A. (2011). Palaeoseismic constraints on Holocene surface ruptures along the Ostler Fault, southern New Zealand. *New Zealand Journal of Geology and Geophysics*, *54*(4), 367–378. https://doi.org/10.1080/00288306.2011.601746

Avouac, J. P., & Leprince, S. (2015). 3.13—Geodetic imaging using optical systems. In G. Schubert (Ed.), *Treatise on geophysics*, (Second ed. pp. 387–424). Oxford: Elsevier. https://doi.org/10.1016/B978-0-444-53802-4.00067-1

Barnhart, W. D., Briggs, R. W., Reitman, N., Gold, R. D., & Hayes, G. P. (2015). Evidence for slip partitioning and bimodal slip behavior on a single fault: Surface slip characteristics of the 2013 Mw7.7 Balochistan, Pakistan earthquake. *Earth and Planetary Science Letters*, *420*, 1–11. https://doi.org/10.1016/j.epsl.2015.03.027

Barnhart, W. D., Gold, R. D., Shea, H. N., Peterson, K. E., Briggs, R. W., & Harbor, D. J. (2019). Vertical coseismic offsets derived from high-resolution stereogrammetric DSM differencing: The 2013 Baluchistan, Pakistan earthquake. *Journal of Geophysical Research: Solid Earth*, *124*(6), 6039–6055. https://doi.org/10.1029/2018jb017107

Berberian, M. (1979). Earthquake faulting and bedding thrust associated with the Tabas-e-Golshan (Iran) earthquake of September 16, 1978. *Bulletin of the Seismological Society of America*, *69*(6), 1861–1887.

Besl, P. J., & McKay, N. D. (1992). Method for registration of 3-D shapes, paper presented at Robotics '91, SPIE.

Bilham, R. (2009). The seismic future of cities. *Bulletin of Earthquake Engineering*, *7*(4), 839–887. https://doi.org/10.1007/s10518-009-9147-0

Bodin, P., & Horton, S. (2004). Source parameters and tectonic implications of aftershocks of the Mw 7.6 Bhuj earthquake of 26 January 2001. *Bulletin of the Seismological Society of America*, *94*(3), 818–827. https://doi.org/10.1785/0120030176

Bowman, J. R. (1992). The 1988 Tennant Creek, northern territory, earthquakes: A synthesis. *Australian Journal of Earth Sciences*, *39*(5), 651–669. https://doi.org/10.1080/08120099208728056

Bowman, J. R., & Barlow, B. C. (1991). *Surveys of the fault scarp of the 1986 Marryat Creek, South Australia, earthquake*, Bureau of Mineral Resources, Geology & Geophysics.

Camacho, A., Vernon, R. H., & Fitz Gerald, J. D. (1995). Large volumes of anhydrous pseudotachylyte in the Woodroffe Thrust, eastern Musgrave Ranges, Australia. *Journal of Structural Geology*, *17*(3), 371–383. https://doi.org/10.1016/0191-8141(94)00069-C

Champion, J., Mueller, K., Tate, A., & Guccione, M. (2001). Geometry, numerical models and revised slip rate for the Reelfoot fault and trishear fault-propagation fold, New Madrid seismic zone. *Engineering Geology*, *62*(1-3), 31–49. https://doi.org/10.1016/S0013-7952(01)00048-5

Clark, D., McPherson, A., Allen, T., & De Kool, M. (2013). Coseismic surface deformation caused by the 23 March 2012 Mw 5.4 Ernabella (Pukatja) earthquake, Central Australia: Implications for fault scaling relations in cratonic settings. *Bulletin of the Seismological Society of America*, *104*(1), 24–39. https://doi.org/10.1785/0120120361

Clark, D., McPherson, A., & Van Dissen, R. (2012). Long-term behaviour of Australian stable continental region (SCR) faults. *Tectonophysics*, *566-567*, 1–30. https://doi.org/10.1016/j.tecto.2012.07.004

Crone, A. J., Machette, M. N., & Bowman, J. R. (1992). Geologica investigations of the 1988 Tennant Creek, Australia, earthquakes; implications for paleoseismicity in stable continental regions, *Report Rep. 2032A*.

Crone, A. J., Machette, M. N., & Bowman, J. R. (1997). Episodic nature of earthquake activity in stable continental regions revealed by palaeoseismicity studies of Australian and North American quaternary faults. *Australian Journal of Earth Sciences*, *44*(2), 203–214. https://doi.org/10.1080/08120099708728304

Dolan, J., Christofferson, S., & Shaw, J. (2003). Recognition of paleoearthquakes on the Puente Hills blind thrust fault, California. *Science*, *300*(5616), 115–118. https://doi.org/10.1126/science.1080593

Edgoose, C., Scrimgeour, I. R., & Close, D. (2004). *Geology of the Musgrave Block, Northern Territory: Also 'Northwestern Musgrave Block Special' explanatory notes*, Northern Territory Geological Survey.

Gold, R. D., Cowgill, E., Wang, X. F., & Chen, X. (2006). Application of trishear fault-propagation folding to active reverse faults: Examples from the Dalong Fault, Gansu Province, NW China. *Journal of Structural Geology*, *28*(2), 200–219. https://doi.org/10.1016/j.jsg.2005.10.006

Gold, R. D., Reitman, N. G., Briggs, R. W., Barnhart, W. D., Hayes, G. P., & Wilson, E. (2015). On- and off-fault deformation associated with the September 2013 Mw7.7 Balochistan earthquake: Implications for geologic slip rate measurements. *Tectonophysics*, *660*, 65–78. https://doi.org/10.1016/j.tecto.2015.08.019

Gordon, F., & Lewis, J. (1968). *The Meckering and Calingiri earthquakes, October 1968 and March 1970*, (p. 228). Perth: Geological Survey of Western Australia.

Gray, H. J., Shobe, C. M., Hobley, D. E. J., Tucker, G. E., Duvall, A. R., Harbert, S. A., & Owen, L. A. (2017). Off-fault deformation rate along the southern San Andreas fault at Mecca Hills, southern California, inferred from landscape modeling of curved drainages. *Geology*, *46*(1), 59–62. https://doi.org/10.1130/G39820.1

Haeussler, P., Schwartz, D. P., Dawson, T. E., Stenner, H. D., Lienkaemper, J. J., Sherrod, B., et al. (2004). Surface rupture and slip distribution of the Denal and Totschunda faults in the 3 November 2002 M 7.9 Earthquake, Alaska. *Bulletin of the Seismological Society of America*, *94*(6B), S23–S52. https://doi.org/10.1785/0120040626

Hamling, I. J., Hreinsdóttir, S., Clark, K., Elliott, J., Liang, C., Fielding, E., et al. (2017). Complex multifault rupture during the 2016 Mw 7.8 Kaikōura earthquake, New Zealand. *Science*, *356*(6334), eaam7194. https://doi.org/10.1126/science.aam7194

Hollingsworth, J., Ye, L., & Avouac, J. P. (2017). Dynamically triggered slip on a splay fault in the Mw 7.8, 2016 Kaikoura (New Zealand) earthquake. *Geophysical Research Letters*, *44*, 3517–3525. https://doi.org/10.1002/2016GL072228

Hudnut, K. W., Shen, Z., Murray, M., McClusky, S., King, R., Herring, T., et al. (1996). Co-seismic displacements of the 1994 Northridge, California, earthquake. *Bulletin of the Seismological Society of America*, *86*(1B), S19–S36.

Kaneko, Y., & Fialko, Y. (2011). Shallow slip deficit due to large strike-slip earthquakes in dynamic rupture simulations with elasto-plastic off-fault response. *Geophysical Journal International*, *186*(3), 1389–1403. https://doi.org/10.1111/j.1365-246X.2011.05117.x

Kelson, K. I., Simpson, G. D., VanArsdale, R. B., Haraden, C. C., & Lettis, W. R. (1996). Multiple late Holocene earthquakes along the Reelfoot fault, central New Madrid seismic zone. *Journal of Geophysical Research - Solid Earth*, *101*(B3), 6151–6170. https://doi.org/10.1029/95JB01815

King, T. R., Quigley, M. C., & Clark, D. (2018). Earthquake environmental effects produced by the Mw 6.1, 20th May 2016 Petermann earthquake, Australia. *Tectonophysics*, *747-748*, 357–372. https://doi.org/10.1016/j.tecto.2018.10.010

Klinger, Y., Michel, R., & King, G. C. P. (2006). Evidence for an earthquake barrier model from Mw ~ 7.8 Kokoxili (Tibet) earthquake slip-distribution. *Earth and Planetary Science Letters*, *242*(3-4), 354–364. https://doi.org/10.1016/j.epsl.2005.12.003

Klinger, Y., Okubo, K., Vallage, A., Champenois, J., Delorme, A., Rougier, E., et al. (2018). Earthquake damage patterns resolve complex rupture processes. *Geophysical Research Letters*, *45*(19), 10,279–210,287. https://doi.org/10.1029/2018GL078842

Kuo, C. H., Huang, J. Y., Lin, C. M., Hsu, T. Y., Chao, S. H., & Wen, K. L. (2018). Strong ground motion and pulse-like velocity observations in the near-fault region of the 2018 Mw 6.4 Hualien, Taiwan, earthquake. *Seismological Research Letters*, *90*(1), 40–50. https://doi.org/10.1785/0220180195

Leprince, S., Ayoub, F., Klinger, Y., & Avouac, J. P. (2007). Co-Registration of Optically Sensed Images and Correlation (COSI-Corr): An operational methodology for ground deformation measurements, paper presented at 2007 IEEE International Geoscience and Remote Sensing Symposium, 23-28 July 2007.

Machette, M. N., Crone, A. J., & Bowman, J. R. (1993). Geologic investigations of the 1986 Marryat Creek, Australia, earthquake; implications for paleoseismicity in stable continental regions, *Report Rep. 2032B*.

Massonnet, D., Rossi, M., Carmona, C., Adragna, F., Peltzer, G., Feigl, K., & Rabaute, T. (1993). The displacement field of the Landers earthquake mapped by radar interferometry. *Nature*, *364*(6433), 138–142. https://doi.org/10.1038/364138a0

Metzger, S., Schurr, B., Ratschbacher, L., Sudhaus, H., Kufner, S. K., Schöne, T., et al. (2017). The 2015 Mw7.2 Sarez strike-slip earthquake in the Pamir interior: Response to the underthrusting of India's western promontory. *Tectonics*, *36*, 2407–2421. https://doi.org/10.1002/2017TC004581

Milliner, C. W. D., Dolan, J. F., Hollingsworth, J., Leprince, S., Ayoub, F., & Sammis, C. G. (2015). Quantifying near-field and off-fault deformation patterns of the 1992 Mw 7.3 Landers earthquake. *Geochemistry, Geophysics, Geosystems*, *16*, 1577–1598. https://doi.org/10.1002/2014GC005693

Moss, R. E. S., & Ross, Z. E. (2011a). Probabilistic fault displacement hazard analysis for reverse faults. *Bulletin of the Seismological Society of America*, *101*(4), 1542–1553. https://doi.org/10.1785/0120100248

Moss, R. E. S., & Ross, Z. E. (2011b). Probabilistic fault displacement hazard analysis for reverse faults probabilistic fault displacement hazard analysis for reverse faults. *Bulletin of the Seismological Society of America*, *101*(4), 1542–1553. https://doi.org/10.1785/0120100248

Nissen, E., Krishnan, A., Arowsmith, J. R., & Saripalli, S. (2012). Three-dimensional surface displacements and rotations from differencing pre- and post-earthquake LiDAR point clouds. *Geophysical Research Letters*, *39*, L16301. https://doi.org/10.1029/2012GL052460

Nissen, E., Maruyama, T., Arrowsmith, J. R., Elliott, J. R., Krishnan, A. K., Oskin, M. E., & Saripalli, S. (2014). Coseismic fault zone deformation revealed with differential lidar: Examples from Japanese ~7 intraplate earthquakes. *Earth and Planetary Science Letters*, *405*(0), 244–256. https://doi.org/10.1016/j.epsl.2014.08.031

Noh, M.-J., & Howat, I. M. (2015). Automated stereo-photogrammetric DEM generation at high latitudes: Surface Extraction with TIN-based Search-space Minimization (SETSM) validation and demonstration over glaciated regions. *GI Science & Remote Sensing*, *52*(2), 198–217. https://doi.org/10.1080/15481603.2015.1008621

Oskin, M., Arrowsmith, J. R., Corona, A. H., Elliott, A. J., Fletcher, J. M., Fielding, E. J., et al. (2012). Near-field deformation from the El Mayor–Cucapah earthquake revealed by differential LIDAR. *Science*, *335*(6069), 702–705. https://doi.org/10.1126/science.1213778

Oskin, M., Perg, L., Blumentritt, D., Mukhopadhyay, S., & Iriondo, A. (2007). Slip rate of the Calico fault: Implications for geologic versus geodetic rate discrepancy in the Eastern California Shear Zone. *Journal of Geophysical Research, B, Solid Earth and Planets*, *112*(B3). https://doi.org/10.1029/2006JB004451

Philip, H., & Meghraoui, M. (1983). Structural analysis and interpretation of the surface deformations of the El Asnam Earthquake of October 10, 1980. *Tectonics*, *2*(1), 17–49. https://doi.org/10.1029/TC002i001p00017

Polcari, M., Albano, M., Atzori, S., Bignami, C., & Stramondo, S. (2018). The causative fault of the 2016 Mwp 6.1 Petermann ranges intraplate earthquake (Central Australia) retrieved by C- and L-band InSAR data. *Remote Sensing*, *10*(8), 1311. https://doi.org/10.3390/rs10081311

Pollard, D. D., & Segall, P. (1987). Theoretical ddisplacements and stresses near fractures In Rock: With applications to faults, joints, veins, dikes, and solution surfaces. In B. K. Atkinson (Ed.), *Fracture mechanics of rock*, (pp. 277–349). London: Academic Press. https://doi.org/10.1016/B978-0-12-066266-1.50013-2

Quigley, M., Clark, D., & Sandiford, M. (2010). Tectonic geomorphology of Australia. *Geological Society, London, Special Publications*, *346*(1), 243–265. https://doi.org/10.1144/sp346.13

Rockwell, T. K., Lindvall, S., Dawson, T., Langridge, R., Lettis, W., & Klinger, Y. (2002). Lateral offsets on surveyed cultural features resulting from the 1999 İzmit and Düzce earthquakes, Turkey. *Bulletin of the Seismological Society of America*, *92*(1), 79–94. https://doi.org/10.1785/0120000809

Scott, C., Champenois, J., Klinger, Y., Nissen, E., Maruyama, T., Chiba, T., & Arrowsmith, R. (2019). 2016 M7 Kumamoto, Japan, earthquake slip field derived from a joint inversion of differential lidar topography, optical correlation, and InSAR surface displacements. *Geophysical Research Letters*, *46*. https://doi.org/10.1029/2019gl082202

Shean, D. E., Alexandrov, O., Moratto, Z. M., Smith, B. E., Joughin, I. R., Porter, C., & Morin, P. (2016). An automated, open-source pipeline for mass production of digital elevation models (DEMs) from very-high-resolution commercial stereo satellite imagery. *ISPRS Journal of Photogrammetry and Remote Sensing*, *116*, 101–117. http://doi.org/10.1016/j.isprsjprs.2016.03.012

Simons, M., Fialko, Y., & Rivera, L. (2002). Coseismic deformation from the 1999 Mw 7.1 Hector Mine, California, earthquake as inferred from InSAR and GPS observations. *Bulletin of the Seismological Society of America*, *92*(4), 1390–1402. https://doi.org/10.1785/0120000933

Streig, A. R., Rubin, C. M., Chen, W.-S., Chen, Y.-G., Lee, L.-S., Thompson, S. C., et al. (2007). Evidence for prehistoric coseismic folding along the Tsaotun segment of the Chelungpu fault near Nan-Tou, Taiwan. *Journal of Geophysical Research - Solid Earth*, *112*(B3). https://doi.org/10.1029/2006jb004493

Tregoning, P. (2003). In R. R. Hillis, & R. D. Müller (Eds.), *Is the Australian Plate deforming? A space geodetic perspective*. Geological Society of America.

Van Dissen, R., Hornblow, S., Quigley, M., Litchfield, N., Villamor, P., Nicol, A., et al. (2013). Towards the development of design curves for characterising distributed strike-slip surface fault rupture displacement: An example from the 4 September, 2010, Greendale Fault rupture, New Zealand, paper presented at 19th NZGS Geotechnical Symposium, Citeseer.

Wang, S., Xu, W., Xu, C., Yin, Z., Bürgmann, R., Liu, L., & Jiang, G. (2019). Changes in groundwater level possibly encourage shallow earthquakes in central Australia: The 2016 Petermann Ranges earthquake. *Geophysical Research Letters*, *46*(6), 3189–3198. https://doi.org/10.1029/2018gl080510

Wells, D. L., & Coppersmith, K. J. (1994). New empirical relationships among magnitude, rupture length, rupture width, rupture area, and surface displacement. *Bulletin of the Seismological Society of America*, *84*(4), 974–1002.

Xu, X., Wen, X., Yu, G., Chen, G., Klinger, Y., Hubbard, J., & Shaw, J. (2009). Coseismic reverse-and oblique-slip surface faulting generated by the 2008 Mw 7.9 Wenchuan earthquake, China. *Geology*, *37*(6), 515–518. https://doi.org/10.1130/G25462A.1

Zhou, Y., Parsons, B. E., & Walker, R. T. (2018). Characterizing complex surface ruptures in the 2013 Mw 7.7 Balochistan earthquake using three-dimensional displacements. *Journal of Geophysical Research: Solid Earth*, *123*(11), 10,191–10,211. https://doi.org/10.1029/2018JB016043

Zinke, R., Hollingsworth, J., & Dolan, J. F. (2014). Surface slip and off-fault deformation patterns in the 2013 MW 7.7 Balochistan, Pakistan earthquake: Implications for controls on the distribution of near-surface coseismic slip. *Geochemistry, Geophysics, Geosystems*, *15*, 5034–5050. https://doi.org/10.1002/2014GC005538